Article

Wurtzite Gallium Phosphide via Chemical Beam Epitaxy: Impurity-Related Luminescence vs Growth Conditions

Bruno César da Silva, Odilon Divino Damasceno Couto, Jr., Hélio Obata, Carlos Alberto Senna, Braulio Soares Archanjo, Fernando Iikawa, and Mônica Alonso Cotta*

Read Online

ACCESS | Metrics & More | Article Recommendations | Supporting Information

ABSTRACT: The metastable wurtzite crystal phase in gallium phosphide (WZ GaP) is a relatively new structure with little available information about its emission properties compared to the most stable zinc-blend phase. Here, the effect of growth conditions of WZ GaP nano- and microstructures obtained via chemical beam epitaxy on the optical properties was studied using power- and temperature-dependent photoluminescence (PL). We showed that the PL spectra are dominated by two strong broad emission bands at 1.68 and 1.88 eV and two relatively narrow peaks at 2.04 and 2.09 eV. The broad emissions are associated with the presence of carbon and a small number of extended crystal defects, respectively. For the sharp emissions, two main radiative recombination channels were observed with ionization energies estimated in the range of 50−80 meV and lower than 10 meV. No variation of the low-temperature PL spectra was observed for samples grown at different P precursor flows, while increasing Ga content enhanced the dominant broad emission at around 1.68 eV, suggesting that the group III organometallic precursor is the main source of impurities. Finally, Be-doped samples were grown, and their characteristic optical emission at 2.03 eV was identified. These results contribute to the understanding of impurity-related luminescence in hexagonal GaP, being useful for further crystal growth optimization required for the fabrication of optoelectronic devices.
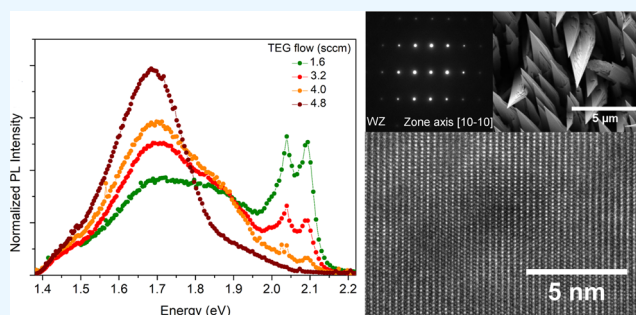
1. INTRODUCTION

Crystal structure switching offers a route to modify and control the optical properties of well-known III−V semiconductors and, therefore, to develop more efficient solid-state optoelectronic devices.[1−3] The Wurtzite (WZ) phase in GaP is made possible at the nanoscale in the form of nanowires (NWs).[4−7] Special attention has been dedicated to the hexagonal crystal structure GaP NWs, where a pseudodirect band gap at 2.19 eV was observed[6,8] as well as a few sharp emissions in the visible spectral range.[4,6,9] In many cases, the dominant optical emissions observed in photoluminescence spectra are attributed to residual impurities or defects,[4,10−12] and few reports so far have focused on understanding the origin of these emissions and their dependence on the growth conditions and techniques.

Impurities generating deep energy levels in semiconductors have been used to obtain semi-insulating materials, but they can also act as undesired optical recombination centers. Impurity-related deep levels may negatively affect materials' properties, such as the case of diminished carrier mobility observed for gold in silicon,[13] or generate optical emissions, reducing band-to-band transitions, such as the yellow band reported for Ga vacancies in GaN.[14,15] In organometallic-based vapor-phase growth systems, carbon originating from the

pyrolysis of the precursors is expected to be the main contaminant.[16,17] However, other different residual impurities may also be incorporated, usually associated with the purity levels of the organometallic source.[18−23] In zinc-blend (ZB) GaP films, many chemical impurities are optically active.[24−29] Among them, nitrogen is one of the most interesting.[30] This impurity acts as an isoelectronic trap in ZB GaP, leading to green emission at room temperature.[31] Despite its low efficiency, this emission was successfully exploited for the fabrication of commercial green light-emitting diodes (LEDs) in the early years of semiconductor research and development.[32]

In metallorganic vapor-phase epitaxy-grown (MOVPE) WZ GaP NWs, using atom probe tomography (APT) Assali et al. showed that C was the only measurable residual impurity.[6] This shows the difficulty of measuring such low levels of impurities even with advanced techniques,[33−35] which are also
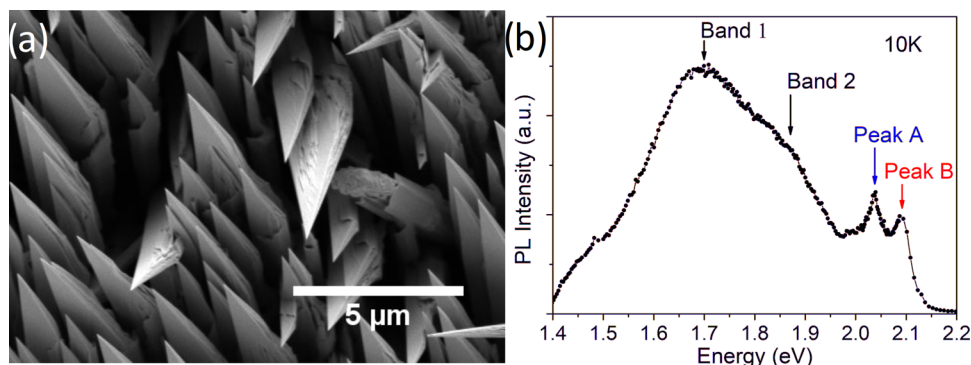
Figure 1. (a) SEM image of large asymmetric WZ GaP structures with an average length of 40 μm and a diameter of up to 3 μm. (b) Typical PL spectrum (acquired at 10 K) of WZ GaP structures under low excitation density (8.0 W/cm^2). The main emissions are named band 1 ($\sim$1.68 eV), band 2 ($\sim$1.88 eV), peak A (2.04 eV), and peak B (2.09 eV).

not widely available. Furthermore, APT is not sensitive to point defects in the material, such as vacancies or antisites. A traditional and noninvasive technique to study impurities in semiconductor materials is photoluminescence (PL). Despite its limited spatial resolution, PL was extensively exploited in the early years of semiconductor research, especially for GaP.[24−33] PL measurements provide a means for a quick evaluation of material quality since luminescence in general is very sensitive to small concentrations of foreign atoms or point defects.

In this work, we have investigated impurity-related optical emissions of Au-seeded asymmetric wurtzite GaP nano- and microstructures grown by chemical beam epitaxy (CBE) under different growth conditions for doped and undoped structures. Electron microscopy was employed to assess the structural properties. Power- and temperature-dependent PL was used to estimate the ionization energies associated with narrow emissions, further elucidating the optical properties of WZ GaP structures.

2. METHODS

The nano- and microstructures were grown by CBE using 5 nm colloidal Au nanoparticles as catalysts, deposited on GaAs (100) substrates. The growth protocol for obtaining the asymmetric morphology in the WZ phase and growth details are described elsewhere.[12] Briefly, triethylgallium (TEG) with H_2 as the carrier gas and thermally cracked phosphine (PH_3) were used as the source of group III and V elements, respectively. Two sets of samples were investigated. In one set, TEG flow was varied from 1.6 to 4.8 sccm with PH_3 flow fixed at 15 sccm. For the other, TEG was fixed at 2.4 sccm and PH_3 flow was varied in the range from 7.5 to 42.5 sccm. Be-doped GaP nanostructures were obtained using the same growth procedure of undoped samples, with Be effusion cell temperatures at 750, 800, and 850 °C. For all samples, prior to growth, the substrates were annealed in vacuum (10^{-5} Torr) at 510 °C for 5 min to allow for nanoparticle crawling.[12] Subsequently, the growth was initiated at the same temperature for 60 min, except when noted otherwise. All samples were cooled down under 15 sccm PH_3 overpressure. Arrays of GaP nanostructures were also grown in the same conditions described in a previous publication[12] using Au nanodots (diameter $\sim$20 nm) spaced by 1−3 μm. The nanodot arrays were prepared by electron beam lithography (EBL) and 5 nm thick thermally evaporated Au films. At last, to enhance the PL

signal, a large microsized WZ GaP structure grown with much longer times, as reported previously,[8] was also analyzed.

The morphological analysis was carried out by field-emission scanning electron microscopy (SEM, Inspect F-50). Transmission electron microscopy (TEM) using a Titan Cubed Themis (FEI) operating at 300 kV was used for structural analysis. A cross-section lamella along the c-axis of the large WZ GaP structure was prepared by focused ion beam (FIB, Helios Nano Lab 650), as indicated in Supporting Information Figure S1.

Optical characterization of the ensemble of the nanostructures in as-grown samples was performed by PL at low temperatures using a 405 nm laser as an excitation source, a double monochromator (SPEX) with 1200 g/mm grating, and a GaAs photocathode photomultiplier for detection. The microsized WZ GaP structures were transferred to a Si substrate for single-nanowire micro-photoluminescence (μ-PL) analysis. In this case, the excitation source was a 488 nm solid-state laser with a 50× objective lens and a single configuration of a Jobin-Yvon monochromator (model 64,000) with 1800 g/mm grating coupled to an LN$_2$-cooled Si CCD for PL detection.

3. RESULTS

3.1. Optical Spectrum of Wurtzite GaP. Figure 1a,b shows a SEM image of the as-grown sample with WZ GaP microstructures and the typical low-temperature macro-PL spectrum obtained at a low-excitation-intensity regime (8.0 W/cm^2). The same overall spectrum is obtained for samples grown in the same conditions but with nanoscale dimensions.[12] The spectrum is dominated by two main broad emissions below 2.0 eV (FWHM $\sim$150 meV) and two relatively narrow (FWHM $\sim$30 meV) peaks at 2.04 and 2.09 eV. Throughout the discussion, we will refer to these main emissions as band 1 ($\sim$1.68 eV), band 2 ($\sim$1.88 eV), peak A (2.04 eV), and peak B (2.09 eV) (see Figure 1b). It is important to mention that the A and B peak energies do not change for different positions along the sample; however, their intensities occasionally vanish, probably due to fluctuations in impurity concentration along the samples. On the other hand, the peak energy for the broader bands 1 and 2 varies slightly at around 1.88 and 1.68 eV. The two broad bands below 2.0 eV are always observed, regardless of the analyzed region on the samples.

Similar PL spectra are also obtained in our μ-PL measurements from single microstructures (Supporting Information
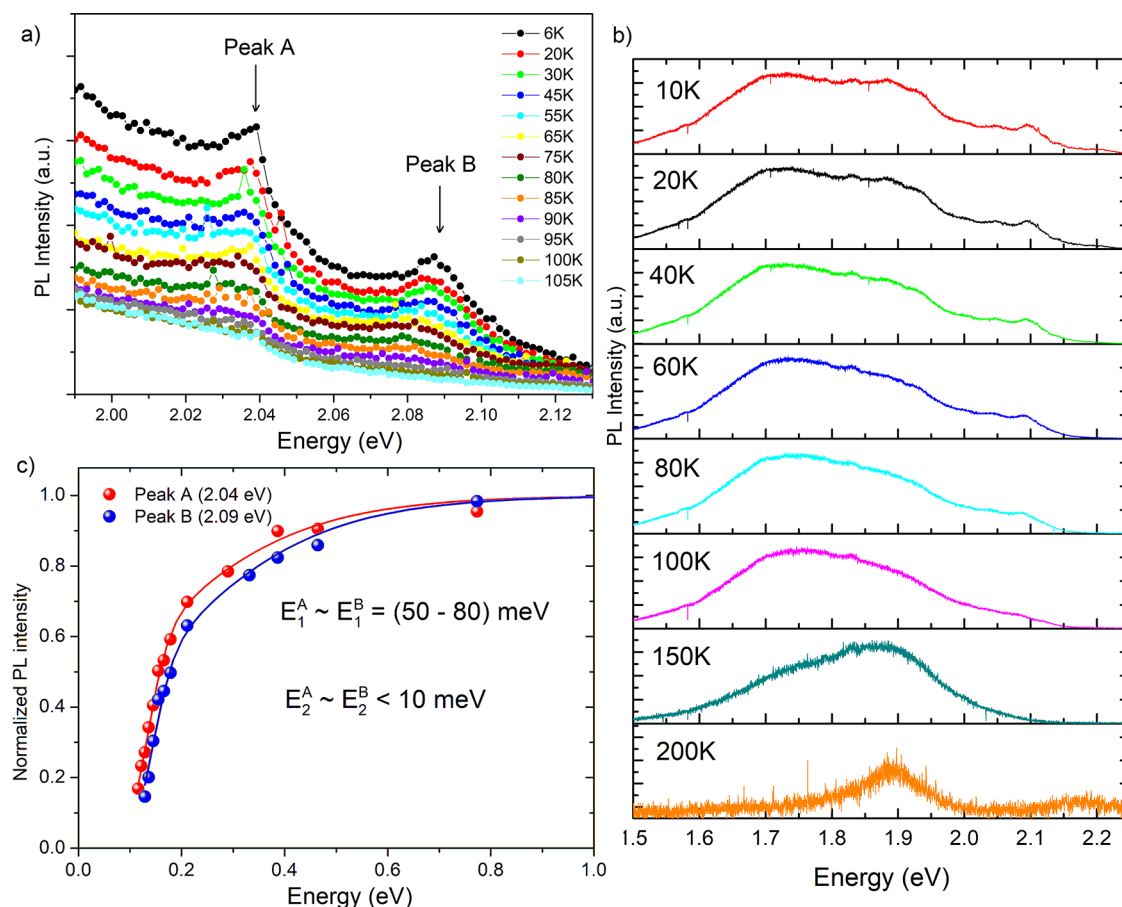
Figure 2. (a) Temperature-dependent PL spectra of a single WZ GaP microstructure acquired under low excitation density (8.0 W/cm^2) showing A and B emissions. (b) Temperature-dependent μ-PL spectra of a single WZ GaP microstructure acquired under low excitation density. (c) Integrated μ-PL intensity of peaks A (2.04 eV) and B (2.09 eV) as a function of the reciprocal temperature with corresponding Arrhenius curves and activation energies.

Figure S2). This is evidence that the macro-PL spectra of as-grown samples are indeed representative of the microstructures and that emissions from the deposited film and substrate are negligible. WZ GaP NWs are also grown using lithographically fabricated Au nanodot arrays (Support Information Figure S3). The typical macro-PL spectrum of these samples is presented in Supporting Information Figure S4. In this case, emission bands below 2.0 eV dominate the spectrum and peaks A and B are not observed.

3.2. Temperature-Dependent PL Measurements. The μ-PL spectra of single microstructures show fast quenching of A and B peaks above 100 K, Figure 2a. Quenching of band 1 emission follows at higher temperatures, and the spectra are dominated by emission band 2 at temperatures above ∼150 K (Figure 2b). This suggests that at least one recombination channel involved in band 1 emission has a lower ionization energy than those involved in band 2. The quenching of both sharp A and B peaks at temperatures ∼100 K suggests that they are both related to shallower impurities when compared to bands 1 and 2.

The ionization energies for the impurities associated with the sharp peaks were estimated by the Arrhenius plot of the integrated PL intensity shown in Figure 2c. The integrated intensity of peaks A and B was obtained by deconvolution using Gaussian functions after removal of the background generated by the emissions below 2.0 eV. The position of peak A, close to the tail of the broad emission, increased the

uncertainty of the analysis due to background removal. Here, we used a fixed Gaussian centered at the 1.88 eV emission as the background for peak A deconvolution, while only an offset was removed as the background for peak B.

The best fit for the narrow A and B peaks was obtained using two radiative recombination channels, as shown in eq (1).

$$I = \frac{I_0}{1 + C_1^{A,B}\, e^{-E_1^{A,B}/k_B T} + C_2^{A,B}\, e^{-E_2^{A,B}/k_B T}} \tag{1}$$

In eq 1, k_B is the Boltzmann constant, C_1^A (C_1^B) and C_2^A (C_2^B) are constants, and E_1^A (E_1^B) and E_2^A (E_2^B) are the thermal activation energies of the impurities involved in the emission of peak A (peak B). Both peaks show similar values and uncertainties for the pair of ionization energies. The obtained values are $E_1^A \cong E_1^B = (50-80)$ meV and $E_2^A \cong E_2^B < 10$ meV.

3.3. Power-Dependent PL Measurements. When we analyze the excitation power dependence of the PL spectra, two distinct behaviors can be noticed. At intermediate excitation powers, peaks A and B saturate, while bands 1 and 2 do not, Figure 3a,b. Thus, impurities or crystal defects associated with emissions below 2.0 eV are most likely present in the sample in larger concentrations than those associated with A and B peaks. A blue shift of a few millielectronvolts and power law behavior with exponents $n = 1$ and $n = 0.9$ for peaks A and B, respectively, were observed (Figure 3c).
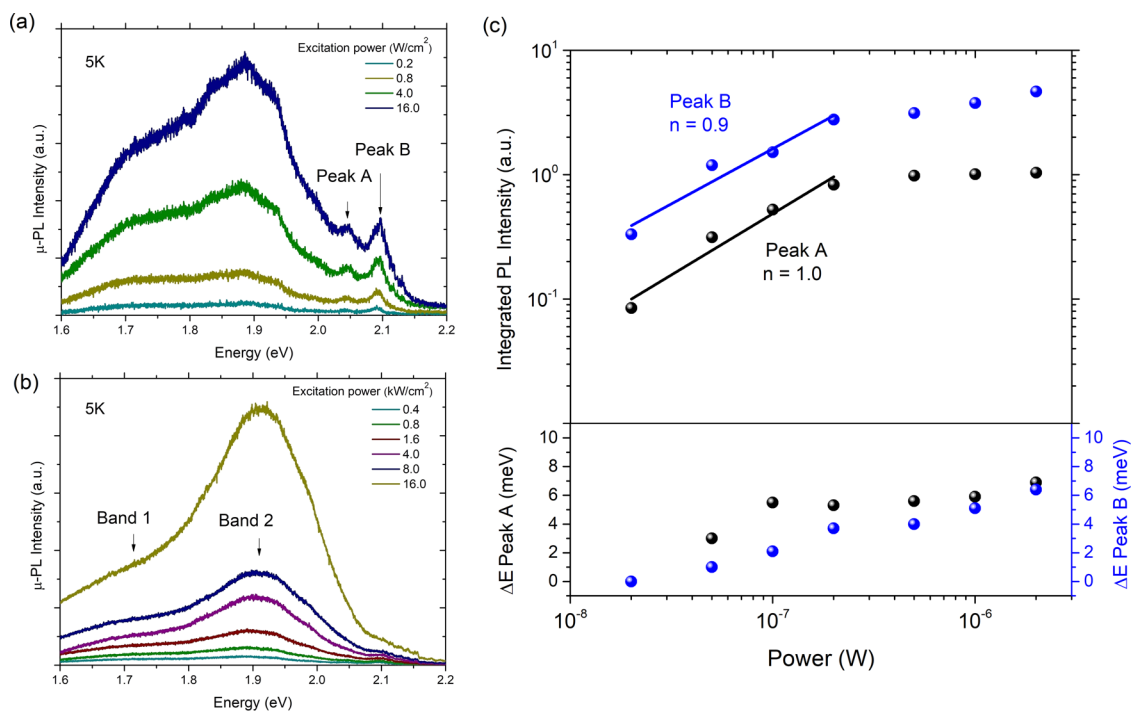
Figure 3. μ-PL spectra of the WZ GaP microstructure acquired at 5 K as a function of the excitation power. (a) Low-power regime ($\leq$0.1 kW/cm^2). (b) High-power regime ($\geq$1 kW/cm^2). (c) Integrated μ-PL intensity and emission energy as a function of the power excitation for A and B peaks in the low-power regime ($\leq$0.1 kW/cm^2).
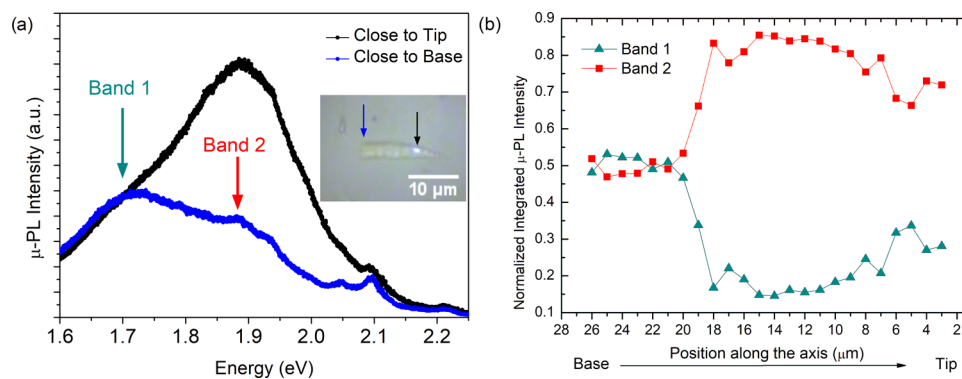

Figure 4. (a) μ-PL spectra (acquired at 5 K) of the large WZ GaP structure under a low-excitation-density regime (8.0 W/cm^2) in different positions along the long axis of the structure. The broad emissions observed below 2.0 eV, band 1 centered at ~1.68 eV and band 2 at ~1.88 eV, are indicated by green and red arrows, respectively. Inset: optical microscopy image of the single WZ GaP structure transferred to a Si substrate, where the measurement was performed. The vertical black and blue arrows indicate the tip and the base positions in corresponding colors to the spectra. (b) Normalized μ-PL intensities (using the integrated PL intensity) of band 1 and band 2 as a function of the position along the structure (the corresponding spectra are presented in Supporting Information Figure S5).

3.4. Position-Dependent PL Measurements.

The incorporation of dopants and defects during vapor—liquid—solid (VLS) growth of semiconductor nanomaterials such as nanowires is strongly affected by two distinct mechanisms: axial VLS and the radial vapor—solid (VS) growth modes. This usually leads to inhomogeneities in the impurities, defect incorporation in a direction perpendicular to the nanowire axis, and formation of a core—shell structure.[34−36] Thus, position-dependent μ-PL spectroscopy of a single microstructure was performed along both short and long axes of the asymmetric GaP microstructure.

Figure 4a depicts two μ-PL spectra measured at the base and the apex of a single GaP microestructure, which clearly show emission bands 1 and 2. Indeed, these bands are present in all

regions of the structure, as shown in Supporting Information Figure S5. As we can see in Figure 4a,b, band 2 intensity is much stronger than that of band 1 around the tip; however, the intensity drops abruptly at ~6 μm from the base in this particular GaP microstructure. It is important to mention that the microstructure has broken in an arbitrary position during transfer to the Si substrate, so we cannot pinpoint how this distance refers to the as-grown substrate. Figure 4b shows the normalized PL intensity to suppress the effects of volume variation along the wire on the PL signal. Four structures analyzed provided different intensity ratios for band 1 and band 2 emissions; however, enhanced band 2 intensity at the tip, as compared to that of band 1, was observed for all measurements. On the other hand, we have not seen drastic

changes in the PL spectra as we scanned the structures across the perpendicular direction, Supporting Information Figure S6a−d.

3.5. Structural Characterizations.
To inspect the crystal structure of these GaP microstructures, we have analyzed the presence of crystal structure defects such as stacking faults or ZB insertions along the GaP structure. Figure 5a,b shows the
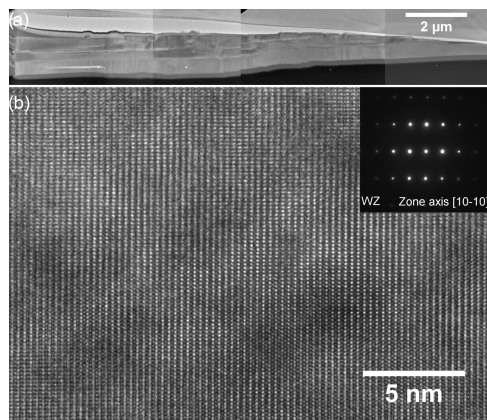

Figure 5. (a) Mosaic of low-magnification TEM image of a lamella prepared from the WZ GaP structure. (b) HRTEM image of the lamella shown in (a); no extended defects were observed in this region. Despite the large volume, the structure presented a good crystal quality; several different points along the structure were analyzed and low extended defect density was observed. Inset: SAED pattern acquired at the base and indexed as WZ in the [10-10] zone axis.

TEM and high-resolution transmission electron microscopy (HRTEM) images of the lamella prepared by FIB and the SAED pattern acquired at the base of the microstructure. A very small number of extended defects was observed when the whole structure was analyzed. Thus, the large GaP microstructure presents a good crystal quality in the WZ phase, as illustrated in the HRTEM image and SAED pattern shown in Figure 5b. The contrast variation in Figure 5a is related to different thickness values due to the lamella preparation process.

3.6. Dependence of PL on Growth Conditions.
We also studied the PL of as-grown samples of asymmetric WZ GaP nanostructures grown under different conditions. First, we investigated the effect of different TEG flows, which directly impact the axial growth rate of these GaP nanostructures.[12] Here, we kept group V flow constant and the V/III ratio was varied via TEG flow. Figure 6a shows the PL spectra of the samples, where the average nanostructure length is about 1 μm (10 μm) for the lowest (highest) TEG flow. The growth rate increases with TEG flow. Thus, all spectra were normalized by the integrated PL intensity to compensate for volume variations in different samples. In Figure 6a, we noticed that band 1 emission (at 1.68 eV) dominated the PL spectra at higher TEG flows and its relative intensity decreased systematically as the TEG flow was reduced. On the other hand, the band 2 relative emission (at 1.88 eV) showed a much less pronounced behavior, except for the highest TEG flow, 4.8 sccm, Figure 6a. No strong variation in the PL spectra was observed under different PH$_3$ flows, Figure S7.

These scenarios for residual impurity incorporation in WZ GaP structures can also be evaluated by introducing a dopant with well-known characteristics and studying how it affects the optical properties of the undoped material. In particular, Be is a shallow acceptor (Be$_{Ga}$) in ZB GaP, with an ionization energy of 50 ± 1 meV.[24,37] Furthermore, doping is a key step for optoelectronic device fabrication. In this context, we have successfully grown Be-doped WZ GaP. The doped samples allowed us to identify the Be ionization energy in hexagonal-phase GaP. The PL spectra as a function of the Be flux (as determined by Be cell temperature) are shown in Figure 6b; the PL spectra are also normalized by the total area to compensate for variations in the GaP volume. The introduction of Be does not affect the growth dynamics, i.e., we still obtain WZ GaP nanostructures with the characteristic asymmetric morphology (inset in Figure 6b). For all PL spectra of Be-doped samples, a significant enhancement of the peak at 2.03 eV is observed, which is very close to peak A in the undoped samples.

4. DISCUSSION

4.1. Sharp Peaks at 2.04 and 2.09 eV and Be Emission at 2.03 eV.
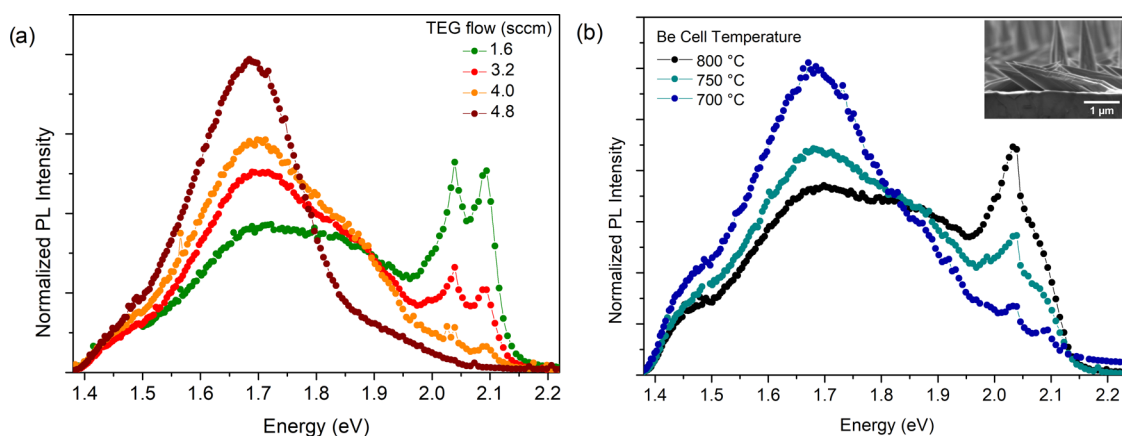Emissions close in energy to those reported here

Figure 6. Normalized PL spectra of WZ GaP nanostructures carried out at 10 K and low excitation density (∼1.5 W/cm^2). (a) WZ GaP nanostructures grown using different TEG flows. (b) Be-doped WZ GaP nanostructures grown for three different Be contents (Be cell temperature). Inset: Side-view SEM image of Be-doped (800 °C) GaP nanostructures. The spectra were normalized by the total area under the curves to suppress volume effects on the analysis of relative intensities of the samples.

have been observed for low-temperature PL measurements in WZ GaP NWs.[4,6,10,12,38] In particular, Maliakkal et al. attributed the emission band at 2.10 eV to defects.[10] An emission band quite close to our peak A, at 2.02 eV, for high-quality WZ GaP NWs grown by MOMBE was also observed by Halder et al., and it was attributed to donor–acceptor pair (DAP) recombination.[38] Assali et al. observed a peak at 2.088 eV and also attributed it to a DAP.

Using the power-dependent measurements, a phenomenological relation can be obtained to tentatively identify the nature of the emissions.[39] Impurity recombinations such as donor–acceptor (D–A) pair and free-to-bound recombinations are associated with a power law dependence with exponent $n \leq 1$,[39,40] while excitonic recombinations present $n \geq 1$.[38] In addition, D–A recombinations are usually followed by a strong blue shift with increasing excitation power.[6] Figure 3c shows that peaks A and B have a moderate blue shift and saturate with excitation power. This means that peak B at 2.09 eV could be assigned as a DAP transition, in agreement with the report of Assali et al.[6] Peak A at 2.04 eV presents a similar behavior in power- and temperature-dependent measurements and could also be interpreted as a DAP recombination. We cannot formally exclude bound excitons as a possible origin for both emissions; however, the power dependence of peaks A and B contrasts with previous measurements of free exciton emission at 2.14 eV, measured in the same sample, but with an excitation power three orders of magnitude higher (>1 kW/cm^2) than in the conditions used to observe peaks A and B in the present study.[8] In such free excitonic emission, no PL intensity variation with power and a sharp emission (FWHM ~1 meV) was observed.[8] Here, peaks A and B present a much broader emission (FWHM of 30 meV) and a clear blue shift.

The obtained values of $E_1^A \cong E_1^B = (50-80)$ meV and $E_2^A \cong E_2^B \leq 10$ meV for peaks A and B are also in agreement with the observations of Assali et al.[6] However, the values obtained for ionization energies (E_2^A and E_2^B) are too small to match the range of common shallow impurities in III–V compounds, and their origin is not clear yet.

Intensities for both A and B peaks are enhanced with low TEG flow and, consequently, lower growth rates, as shown in Figure 6a. Impurity incorporation during vapor-phase epitaxy strongly depends on growth conditions, such as growth rate and V/III ratio;[20,41–43] in particular, residual impurities are more efficiently incorporated under low growth rates. As most of the volume in our asymmetric GaP structures is provided by VS growth, we can expect similarities in impurity incorporation dynamics between thin films and our WZ GaP structures. The increase in peak A and B relative intensities with lower TEG flows is interpreted as an enhancement of impurity incorporation, favored by the lower growth rates. The main impurity in our growth system is C, which originated from the pyrolysis of the organometallic compound used as a Ga precursor. However, the intensity of these emissions can vary along different positions in the sample substrate, suggesting that impurity incorporation is inhomogeneous and associated with a less abundant impurity. The lack of observation of peaks A and B in the structures grown using EBL gold nanoparticles (Figure S4) and their enhancement with the low TEG flow (Figure 6a) indicates that the impurities associated with those peaks come probably from the group III organometallic precursor or the colloidal gold nanoparticles. Therefore, based on our power-dependent PL measurements, we also attribute

A and B emissions to residual impurities forming a D–A recombination centers.

The emission at 2.03 eV can be unambiguously attributed to Be dopant, as we can see in Figure 6b. We cannot distinguish the Be-related and peak A emissions in Figure 6b. The peak at 2.03 eV does not present a blue shift (Figure 6b) with increasing Be content. This is an indication that DAP recombination may not explain the emission at 2.03 eV. Using the estimated band gap of the WZ GaP at 2.19 eV,[8] we can tentatively attribute this emission to band-acceptor recombination and estimate the ionization energy for Be in the WZ phase as approximately 160 meV. In contrast, the ionization energy of Be as an acceptor in ZB GaP is 50 meV.[24] However, we cannot rule out DAP recombination since peaks A and B also do not present a blue shift with reduced TEG flow.

4.2. Broad Band Emission at 1.68 and 1.88 eV. Figure 5 shows that the sample grown at high TEG flow (4.8 sccm, with PH$_3$ 20 sccm) presents relatively good crystal quality with a low density of extended defects. However, a low density of stacking faults can still be expected. In Figure 3a,b, the emissions of bands 1 and 2 do not saturate with power, suggesting that these bands are related to a more abundant source, as compared to the case of peaks A and B. Assali et al. have observed emissions similar to band 1 and attributed them to incorporated impurities, while band 2 was assigned to type II ZB/WZ junctions.[4] Figure 4 shows that band 2 dominates the PL at the tip of the microstructure. Thus, Figure 4 suggests that this specific microstructure has a better crystal quality at the base. This is not a general rule since a different trend is observed in Figure S6. In Figures S5 and S6, we can see that the relative intensity between band 1 and band 2 varies only axially, indicating the connection of band 2 with the density of stacking faults.

Band 1 should be associated with a different mechanism because the emission at 1.68 eV quenches before that at 1.88 eV, suggesting that the emission at 1.68 eV has at least one shallower state when compared to band 2. We can see in Figure 6a that increasing the TEG flow enhances band 1 relative emission, while band 2 intensity remains reasonably constant, except for the highest TEG flow used. Thus, we propose that carbon is the shallow impurity involved in band 1 transition, most likely a DAP, with the deep donor unknown so far.

4.3. Residual Impurity Growth Dynamics. In Figure 6a, we can see that the relative enhancement of the narrow peaks in the yellow/amber spectral range, 2.04–2.09 eV, can be observed for lower group III flows. The spectrum shown in Figure 6a for the growth carried out under the lowest TEG flow (1.6 sccm) resembles the data reported by Assali et al.,[4] where they initially assigned the emission at 2.09 eV (peak B) to the band gap transition. Despite the specific growth condition displayed by Assali et al., other samples have been reported with the suppression of deep-level emissions below 2.0 eV, but the understanding of growth mechanisms related to that behavior has not yet been discussed.[6,44] The results presented here can represent a more general trend for the growth of WZ GaP using other epitaxy systems as, for example, MOMBE systems that use organometallic sources. The CBE technique used here employs chemical compounds (containing the elements of interest) in the vapor phase as precursors, similar to the MOVPE technique, allowing precise control over their flow. However, the CBE growth is performed in high

vacuum, as in a MBE system, allowing better control over the growth of atomic layer interfaces. It is interesting to note that Hadler et al.[38] reported emissions at 2.02 and 2.13 eV in high-quality WZ GaP NWs grown by MOMBE, while Assali et al.[4,6] have observed similar emission as reported here. The differences observed in the impurity-related emissions may be related to the different gold catalysts used in each study. Regardless of the impurity source, the results demonstrated here may represent a pathway for other organometallic-based epitaxy techniques to modify residual impurity incorporation and, consequently, improve the crystal quality of the grown hexagonal GaP structure.

5. CONCLUSIONS

In conclusion, we have studied the optical properties of micro- and nanostructures of WZ GaP with low density of extended crystal defects. Their emissions are dominated by impurity-related luminescence, with two broad bands below 2.0 eV, at around 1.68 and 1.88 eV. These are associated with the presence of carbon and a small number of extended crystal defects, respectively. Two relatively narrow emissions in the amber/yellow spectral range are also reported, at 2.04 and 2.09 eV. It is shown that they are associated with recombination channels with two ionization energies, one smaller than 10 meV and a second one in the range of 50−80 meV, which are most likely associated with DAP emissions. A strong dependence of these peaks with TEG flow is also reported, suggesting that a lower content of unintentionally incorporated impurities comes from the group III organometallic precursor. A clear emission at 2.03 eV associated with Be doping is also observed.

A better understanding of the optical emissions present in the hexagonal GaP is crucial for further control of material quality and device fabrication. The results presented here provide the first assessment of the luminescence of the unexplored hexagonal GaP caused by residual impurities and/or native defects synthesized by an organometallic-based vapor-phase technique.

ASSOCIATED CONTENT

SI Supporting Information

The Supporting Information is available free of charge at https://pubs.acs.org/doi/10.1021/acsomega.2c05666.

> Additional SEM images, PL and μ-PL measurements, and analyses (PDF)

AUTHOR INFORMATION

Corresponding Author

Mônica Alonso Cotta − Institute of Physics "Gleb Wataghin", University of Campinas, 13083-859 Campinas, São Paulo, Brazil; ● orcid.org/0000-0002-2779-5179; Email: monica@ifi.unicamp.br

Authors

Bruno César da Silva − Institute of Physics "Gleb Wataghin", University of Campinas, 13083-859 Campinas, São Paulo, Brazil; Present Address: University Grenoble Alpes, CNRS-Institut Néel, F-38000 Grenoble, France; ● orcid.org/0000-0001-8690-4796

Odilon Divino Damasceno Couto, Jr. − Institute of Physics "Gleb Wataghin", University of Campinas, 13083-859 Campinas, São Paulo, Brazil; ● orcid.org/0000-0002-8416-3805

Hélio Obata − Institute of Physics "Gleb Wataghin", University of Campinas, 13083-859 Campinas, São Paulo, Brazil

Carlos Alberto Senna − Materials Metrology Division, National Institute of Metrology, Quality and Technology, 25250-020 Duque de Caxias, Rio de Janeiro, Brazil

Braulio Soares Archanjo − Materials Metrology Division, National Institute of Metrology, Quality and Technology, 25250-020 Duque de Caxias, Rio de Janeiro, Brazil; ● orcid.org/0000-0001-8145-7712

Fernando Iikawa − Institute of Physics "Gleb Wataghin", University of Campinas, 13083-859 Campinas, São Paulo, Brazil

Complete contact information is available at:
https://pubs.acs.org/10.1021/acsomega.2c05666

Notes

The authors declare no competing financial interest.

ACKNOWLEDGMENTS

REFERENCES

(1) Wallentin, J.; Anttu, N.; Asoli, D.; Huffman, M.; Åberg, I.; Magnusson, M. H.; Siefer, G.; Fuss-Kailuweit, P.; Dimroth, F.; Witzigmann, B.; Xu, H. Q.; Samuelson, L.; Deppert, K.; Borgström, M. T. InP Nanowire Array Solar Cells Achieving 13.8% Efficiency by Exceeding the Ray Optics Limit. *Science* 2013, 339, 1057−1060.

(2) Philip, M. R.; Choudhary, D. D.; Djavid, M.; Le, K. Q.; Piao, J.; Nguyen, H. P. T. High Efficiency Green/Yellow and Red InGaN/AlGaN Nanowire Light-Emitting Diodes Grown by Molecular Beam Epitaxy. *J. Sci.: Adv. Mater. Devices* 2017, 2, 150−155.

(3) Krogstrup, P.; Jørgensen, H. I.; Heiss, M.; Demichel, O.; Holm, J. V.; Aagesen, M.; Nygård, J.; Fontcuberta I Morral, A. Single-Nanowire Solar Cells beyond the Shockley-Queisser Limit. *Nat. Photonics* 2013, 7, 306−310.

(4) Assali, S.; Zardo, I.; Plissard, S.; Kriegner, D.; Verheijen, M. A.; Bauer, G.; Meijerink, A.; Belabbes, A.; Bechstedt, F.; Haverkort, J. E. M.; Bakkers, E. P. A. M. Direct Band Gap Wurtzite Gallium Phosphide Nanowires. *Nano Lett.* 2013, 13, 1559−1563.

(5) Standing, A.; Assali, S.; Gao, L.; Verheijen, M. A.; van Dam, D.; Cui, Y.; Notten, P. H. L.; Haverkort, J. E. M.; Bakkers, E. P. A. M. Efficient Water Reduction with Gallium Phosphide Nanowires. *Nat. Commun.* 2015, 6, No. 7824.

(6) Assali, S.; Greil, J.; Zardo, I.; Belabbes, A.; de Moor, M. W. A.; Koelling, S.; Koenraad, P. M.; Bechstedt, F.; Bakkers, E. P. A. M.; Haverkort, J. E. M. Optical Study of the Band Structure of Wurtzite GaP Nanowires. *J. Appl. Phys.* 2016, 120, No. 044304.

(7) Hauge, H. I. T.; Verheijen, M. A.; Conesa-Boj, S.; Etzelstorfer, T.; Watzinger, M.; Kriegner, D.; Zardo, I.; Fasolato, C.; Capitani, F.; Postorino, P.; Kölling, S.; Li, A.; Assali, S.; Stangl, J.; Bakkers, E. P. A. M. Hexagonal Silicon Realized. *Nano Lett.* 2015, 15, 5855−5860.

(8) da Silva, B. C.; Couto, O. D. D.; Obata, H. T.; de Lima, M. M.; Bonani, F. D.; de Oliveira, C. E.; Sipahi, G. M.; Iikawa, F.; Cotta, M.

A. Optical Absorption Exhibits Pseudo-Direct Band Gap of Wurtzite Gallium Phosphide. *Sci. Rep.* **2020**, *10*, No. 7904.

(9) Assali, S.; Lähnemann, J.; Vu, T. T. T.; Jöns, K. D.; Gagliano, L.; Verheijen, M. A.; Akopian, N.; Bakkers, E. P. A. M.; Haverkort, J. E. M. Crystal Phase Quantum Well Emission with Digital Control. *Nano Lett.* **2017**, *17*, 6062−6068.

(10) Maliakkal, C. B.; Gokhale, M.; Parmar, J.; Bapat, R. D.; Chalke, B. A.; Ghosh, S.; Bhattacharya, A. Growth, Structural and Optical Characterization of Wurtzite GaP Nanowires. *Nanotechnology* **2019**, *30*, No. 254002.

(11) Berg, A.; Lehmann, S.; Vainorius, N.; Gustafsson, A.; Pistol, M.-E.; Wallenberg, L. R.; Samuelson, L.; Borgström, M. T. Growth and Characterization of Wurtzite GaP Nanowires with Control over Axial and Radial Growth by Use of HCl In-Situ Etching. *J. Cryst. Growth* **2014**, *386*, 47−51.

(12) da Silva, B. C.; Oliveira, D. S.; Iikawa, F.; Couto, O. D. D.; Bettini, J.; Zagonel, L. F.; Cotta, M. A. Exploring Au Droplet Motion in Nanowire Growth: A Simple Route toward Asymmetric GaP Morphologies. *Nano Lett.* **2017**, *17*, 7274−7282.

(13) Tavendale, A. J.; Pearton, S. J. Deep Level, Quenched-in Defects in Silicon Doped with Gold, Silver, Iron, Copper or Nickel. *J. Phys. C: Solid State Phys.* **1983**, *16*, 1665−1673.

(14) Neugebauer, J.; Van de Walle, C. G. Gallium Vacancies and the Yellow Luminescence in GaN. *Appl. Phys. Lett.* **1996**, *69*, 503−505.

(15) Ogino, T.; Aoki, M. Mechanism of Yellow Luminescence in GaN. *Jpn. J. Appl. Phys.* **1980**, *19*, 2395−2405.

(16) Brozel, M. R.; Newman, R. C.; Clegg, J. B. Carbon, Oxygen and Silicon Impurities in Gallium Arsenide. *J. Phys. Appl. Phys.* **1978**, *11*, 1331−1339.

(17) Watkins, S. P.; Haacke, G. Carbon Acceptor Incorporation in GaAs Grown by Metalorganic Chemical Vapor Deposition: Arsine versus Tertiarybutylarsine. *Appl. Phys. Lett.* **1991**, *59*, 2263−2265.

(18) Seki, Y.; Tanno, K.; Iida, K.; Ichiki, E. Properties of Epitaxial GaAs Layers from a Triethyl Gallium and Arsine System. *J. Electrochem. Soc.* **1975**, *122*, 1108−1112.

(19) Dapkus, P. D.; Manasevit, H. M.; Hess, K. L.; Low, T. S.; Stillman, G. E. High Purity GaAs Prepared from Trimethylgallium and Arsine. *J. Cryst. Growth* **1981**, *55*, 10−23.

(20) van de Ven, J.; Schoot, H. G.; Giling, L. J. Influence of Growth Parameters on the Incorporation of Residual Impurities in GaAs Grown by Metalorganic Chemical Vapor Deposition. *J. Appl. Phys.* **1986**, *60*, 1648−1660.

(21) Hata, M.; Fukuhara, N.; Zempo, Y.; Isemura, M.; Yako, T.; Maeda, T. Residual Impurities in Epitaxial Layers Grown by MOVPE. *J. Cryst. Growth* **1988**, *93*, 543−549.

(22) Roth, A. P.; Charbonneau, S.; Goodchild, R. G. Residual Shallow Acceptors in GaAs Layers Grown by Metal-Organic Vapor Phase Epitaxy. *J. Appl. Phys.* **1983**, *54*, 5350−5357.

(23) Hanna, M. C.; Lu, Z. H.; Oh, E. G.; Mao, E.; Majerfeld, A. Intrinsic Carbon Incorporation in Very High Purity MOVPE GaAs. *J. Cryst. Growth* **1992**, *124*, 443−448.

(24) Dean, P. J.; Ilegems, M. The Optical Properties of Be, Mg and Zn-Diffused Gallium Phosphide. *J. Lumin.* **1971**, *4*, 201−230.

(25) Dean, P. J.; Schönherr, E. G.; Zetterstrom, R. B. Pair Spectra Involving the Shallow Acceptor Mg in GaP. *J. Appl. Phys.* **1970**, *41*, 3475−3479.

(26) Demidov, D. M.; Zykov, A. M.; Samorukov, B. E. Luminescence of Zinc and Aluminum Doped Gallium Phosphide. *Sov. Phys. J.* **1972**, *15*, 1063−1065.

(27) Leys, M. R.; Pistol, M. E.; Titze, H.; Samuelson, L. On the Growth of Gallium Phosphide Layers on Gallium Phosphide Substrates by MOVPE. *J. Electron. Mater.* **1989**, *18*, 25−31.

(28) Monemar, B. Red Pair Luminescence in GaP:Cu. *J. Lumin.* **1972**, *5*, 472−481.

(29) Hayes, W.; Ryan, J. F.; West, C. L.; Dean, P. J. Photo-luminescence Studies of Deep Traps in GaP:Fe. *J. Phys. C: Solid State Phys.* **1980**, *13*, 5631−5643.

(30) Rauch, C. J.; Stickler, J. J.; Zeiger, H. J.; Heller, G. S. Isoelectronic Traps Due to Nitrogen in Gallium Phosphide. *Phys. Rev. Lett.* **1960**, *4*, 64−66.

(31) Dean, P. J.; Gershenzon, M.; Kaminsky, G. Green Electro-luminescence from Gallium Phosphide Diodes near Room Temperature. *J. Appl. Phys.* **1967**, *38*, 5332−5342.

(32) Wight, D. R. Green Luminescence Efficiency in Gallium Phosphide. *J. Phys. D: Appl. Phys.* **1977**, *10*, 431−454.

(33) Dean, P. J.; Frosch, C. J.; Henry, C. H. Optical Properties of the Group IV Elements Carbon and Silicon in Gallium Phosphide. *J. Appl. Phys.* **1968**, *39*, 5631−5646.

(34) Perea, D. E.; Hemesath, E. R.; Schwalbach, E. J.; Lensch-Falk, J. L.; Voorhees, P. W.; Lauhon, L. J. Direct Measurement of Dopant Distribution in an Individual Vapour-Liquid-Solid Nanowire. *Nat. Nanotechnol.* **2009**, *4*, 315−319.

(35) Sun, Z.; Hazut, O.; Huang, B. C.; Chiu, Y. P.; Chang, C. S.; Yerushalmi, R.; Lauhon, L. J.; Seidman, D. N. Dopant Diffusion and Activation in Silicon Nanowires Fabricated by Ex Situ Doping: A Correlative Study via Atom-Probe Tomography and Scanning Tunneling Spectroscopy. *Nano Lett.* **2016**, *16*, 4490−4500.

(36) Möller, M.; Oliveira, D. S.; Sahoo, P. K.; Cotta, M. A.; Iikawa, F.; Motisuke, P.; Molina-Sánchez, A.; de Lima, M. M.; García-Cristóbal, A.; Cantarero, A. Fermi Energy Dependence of the Optical Emission in Core/Shell InAs Nanowire Homostructures. *Nanotechnology* **2017**, *28*, No. 295702.

(37) Ilegems, M.; O'Mara, W. C. Diffusion of Beryllium into Gallium Phosphide. *J. Appl. Phys.* **1972**, *43*, 1190−1197.

(38) Halder, N. N.; Cohen, S.; Gershoni, D.; Ritter, D. Growth of Large Diameter Pure Phase Wurtzite GaP Nanowires by a Two-Step Axial-Radial Growth Approach. *Appl. Phys. Lett.* **2018**, *112*, No. 133107.

(39) Schmidt, T.; Lischka, K.; Zulehner, W. Excitation-Power Dependence of the near-Band-Edge Photoluminescence of Semi-conductors. *Phys. Rev. B* **1992**, *45*, 8989−8994.

(40) Spindler, C.; Galvani, T.; Wirtz, L.; Rey, G.; Siebentritt, S. Excitation-Intensity Dependence of Shallow and Deep-Level Photo-luminescence Transitions in Semiconductors. *J. Appl. Phys.* **2019**, *126*, No. 175703.

(41) Kuech, T. F.; Potemski, R. Reduction of Background Doping in Metalorganic Vapor Phase Epitaxy of GaAs Using Triethylgallium at Low Reactor Pressures. *Appl. Phys. Lett.* **1985**, *47*, 821−823.

(42) Kuech, T. F.; Veuhoff, E. Mechanism of Carbon Incorporation in MOCVD GaAs. *J. Cryst. Growth* **1984**, *68*, 148−156.

(43) Kerr, T. M.; Wood, C. E. C.; Newstead, S. M.; Wilcox, J. D. On Residual Carbon Acceptors in Molecular-Beam Epitaxial GaAs. *J. Appl. Phys.* **1989**, *65*, 2673−2676.

(44) Greil, J.; Assali, S.; Isono, Y.; Belabbes, A.; Bechstedt, F.; Valega MacKenzie, F. O.; Silov, A. Y.; Bakkers, E. P. A. M.; Haverkort, J. E. M. Optical Properties of Strained Wurtzite Gallium Phosphide Nanowires. *Nano Lett.* **2016**, *16*, 3703−3709.